Available online at www.sciencedirect.com
ScienceDirect
Finite Elements in Analysis and Design 43 (2007) 397–410
FINITE ELEMENTS IN ANALYSIS AND DESIGN
www.elsevier.com/locate/finel

Modeling interfacial debonding and matrix cracking in fiber reinforced composites by the extended Voronoi cell FEM

S. Li, S. Ghosh*

Department of Mechanical Engineering, The Ohio State University, Columbus, OH, USA

Received 10 October 2006; accepted 30 November 2006
Available online 24 January 2007

Abstract

This paper introduces an extended Voronoi cell finite element model (X-VCFEM) for modeling the initiation and propagation of interfacial debonding and matrix cracking in fiber reinforced composite materials. Bilinear and linear cohesive zone models are added for representing interfacial debonding and matrix crack propagation, respectively. A series of criteria based on cohesive zone models are proposed for assessing the direction of damage development, which includes the crack propagation in matrix and its deflection behavior at an interface. Comparisons of X-VCFEM simulations with reference results validate the effectiveness of this new model. The capability of predicting the development of microcracks in composites is of great importance to the design and evaluation of structure. Effect of stereographic features such as size and shape of heterogeneities on damage evolution is also discussed.

Keywords: The extended Voronoi cell finite element method (X-VCFEM); Cohesive zone models; Interfacial debonding; Matrix cracking

1. Introduction

Interfacial debonding and brittle-matrix cracking are two important damage phenomena in fiber-matrix composites. Numerical simulation of the growth and interaction of the two kinds of damages is a challenging topic due to various kinematic and morphological complexities. Conventional finite element approaches suffer from very slow convergence since the element formulation does not account for high gradients and singularities from heterogeneities and damages. Various methods have been proposed for improving the effectiveness of computational methods in modeling damages in composites [1–11]. However, most of these analyses are limited to only one of the two damages analysis.

The Voronoi cell finite element method (VCFEM), developed on the principles of the assumed stress hybrid FEM formulation [6,12], has had considerable success in the micromechanical analysis of multi-phase heterogeneous materials [13–20]. The extended Voronoi cell finite element model (X-VCFEM) has been developed by incorporating the cohesive crack propagation model and special stress functions in VCFEM [13,19,20] to model interfacial debonding in composites and crack propagation in homogenous materials. Computational efficiency of X-VCFEM is substantially higher than many conventional FE models.

This paper discusses how to combine interfacial decohesion and matrix cracking models based on X-VCFEM for fiber-reinforced composite microstructures. The improved X-VCFEM is developed for modeling both the growth of interfacial debonding and the propagation of multiple cohesive cracks in the brittle-matrix composites. Researches regarding a crack meeting a bimaterial interface to either grow along the interface or branch into the next layer were made in [21–24], where the criterion of deflection was established based on the energy release rate and fracture energy. However, the present research is aimed at only elastic cases, which requires that the fracture process zone at the crack tip is small compared to the size of the crack and the size of the specimen. In this paper, a criterion based on cohesive zone models is proposed for assessing the crack growth at the bifurcation point, at which position the cracks branch into matrix from interface.

* Corresponding author. Tel.: +1 614 292 2599; fax: +1 614 292 7369.
E-mail address: ghosh.5@osu.edu (S. Ghosh).

0168-874X/$ - see front matter © 2007 Elsevier B.V. All rights reserved.
doi:10.1016/j.finel.2006.11.010

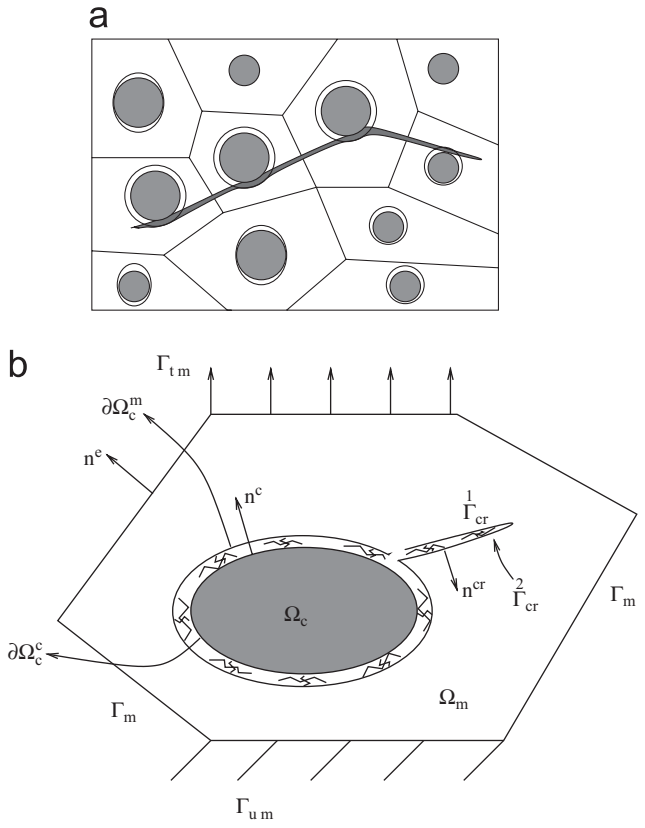

Fig. 1. (a) Voronoi cell mesh for composite microstructure with interface debonding and matrix cracking and (b) a typical Voronoi cell element with interface and crack.

The X-VCFEM formulations are derived, followed by numerical implementations of cohesive zone models and damage growth criteria. Then several numerical examples are used to establish the effectiveness of the model and the interaction of interface and crack propagation is analyzed. The effect of morphological distributions, such as fiber size, shape and orientation, are studied as important factors to the damage process.

2. X-VCFEM formulation for composites with interfacial debonding and matrix cracking

An unstructured mesh for the VCFEM of a composite microstructure is shown in Fig. 1(a). The damaged microstructure considered, consists of both debonded interfaces and cohesive cracks. This is shown in the schematic diagram of a typical VC element Ω_e in Fig. 1(b). Each VC element is composed of the matrix phase (Ω_m), the inclusion phase (Ω_c), the matrix-inclusion interface (Ω_{in}) and cracks (Ω_{cr}), i.e. $\Omega_e = \Omega_m \cup \Omega_c \cup \Omega_{in} \cup \Omega_{cr}$. The interface and cracks are assumed to be zero thickness regions represented by two overlapping surfaces joined by cohesive springs. The element outer boundary consists of the prescribed displacement boundary (Γ_{um}), prescribed traction boundary (Γ_{tm}) and the inter-element boundary (Γ_m), i.e. $\partial\Omega_e = \Gamma_{um} \cup \Gamma_{tm} \cup \Gamma_m$. Compatible displacement conditions are applied on $\partial\Omega_e$. $\partial\Omega_c^c$ has the outward normal $\mathbf{n}^c$ ($= -\mathbf{n}^m$), while $\mathbf{n}^e$ is the outward normal to $\partial\Omega_e$. For describing debonding with progressing deformation due to decohesion, the matrix-inclusion interface is lined with a set of node-pairs, with nodes belonging to the matrix surface ($\partial\Omega_c^m$) and inclusion surface($\partial\Omega_c^c$), respectively. Γ_{intf} corresponds to the interface region between $\partial\Omega_c^m$ and $\partial\Omega_c^c$. The traction $\mathbf{T}^{coh}$ between node-pairs on Γ_{intf} are modeled by a cohesive zone traction-separation law. Brittle cracking in the matrix is also modeled by a cohesive zone model, where nodes in node-pairs are arranged on opposite sides of the crack ($\overset{1}{\Gamma}_{cr}$ and $\overset{2}{\Gamma}_{cr}$). In an incremental assumed stress hybrid X-VCFEM formulation, the complementary energy functional for a VC element is expressed in terms of increments of stress and displacement fields as

$$
\begin{aligned}
&\Pi_e(\boldsymbol{\sigma}, \Delta\boldsymbol{\sigma}, \mathbf{u}, \Delta\mathbf{u}) \\
&= -\int_{\Omega_m} \Delta B(\boldsymbol{\sigma}^m, \Delta\boldsymbol{\sigma}^m)\,d\Omega - \int_{\Omega_c} \Delta B(\sigma^c, \Delta\sigma^c)\,d\Omega \\
&\quad - \int_{\Omega_m} \boldsymbol{\epsilon}^m : \Delta\boldsymbol{\sigma}^m\,d\Omega - \int_{\Omega_c} \boldsymbol{\epsilon}^c : \Delta\boldsymbol{\sigma}^c\,d\Omega \\
&\quad + \int_{\partial\Omega_e} (\boldsymbol{\sigma}^m + \Delta\boldsymbol{\sigma}^m)\cdot\mathbf{n}^e\cdot(\mathbf{u}^e + \Delta\mathbf{u}^e)\,d\partial\Omega \\
&\quad - \int_{\Gamma_{tm}} (\bar{\mathbf{t}} + \Delta\bar{\mathbf{t}})\cdot(\mathbf{u}^m + \Delta\mathbf{u}^m)\,d\Gamma \\
&\quad - \int_{\partial\Omega_c^m} (\boldsymbol{\sigma}^m + \Delta\boldsymbol{\sigma}^m)\cdot\mathbf{n}^c\cdot(\mathbf{u}^m + \Delta\mathbf{u}^m)\,d\partial\Omega \\
&\quad + \int_{\partial\Omega_c^c} (\boldsymbol{\sigma}^c + \Delta\boldsymbol{\sigma}^c)\cdot\mathbf{n}^c\cdot(\mathbf{u}^c + \Delta\mathbf{u}^c)\,d\partial\Omega \\
&\quad + \int_{\overset{1}{\Gamma}_{cr}} (\boldsymbol{\sigma}^m + \Delta\boldsymbol{\sigma}^m)\cdot\mathbf{n}^{cr}\cdot(\overset{1}{\mathbf{u}}^{cr} + \Delta\overset{1}{\mathbf{u}}^{cr})\,d\Gamma_{cr} \\
&\quad - \int_{\overset{2}{\Gamma}_{cr}} (\boldsymbol{\sigma}^m + \Delta\boldsymbol{\sigma}^m)\cdot\mathbf{n}^{cr}\cdot(\overset{2}{\mathbf{u}}^{cr} + \Delta\overset{2}{\mathbf{u}}^{cr})\,d\Gamma_{cr} \\
&\quad - \boxed{\int_{\Gamma_{intf}} \int_{(\mathbf{u}^m - \mathbf{u}^c)}^{(\mathbf{u}^m + \Delta\mathbf{u}^m - \mathbf{u}^c - \Delta\mathbf{u}^c)} \mathbf{T}^i \cdot d(\mathbf{u}^m - \mathbf{u}^c)\,d\partial\Omega} \\
&\quad - \boxed{\int_{\Gamma_{cr}} \int_{\overset{1}{\mathbf{u}}^{cr} - \overset{2}{\mathbf{u}}^{cr}}^{\overset{1}{\mathbf{u}}^{cr} + \Delta\overset{1}{\mathbf{u}}^{cr} - \overset{2}{\mathbf{u}}^{cr} - \Delta\overset{2}{\mathbf{u}}^{cr}} \mathbf{T}^{cr} \cdot d(\overset{1}{\mathbf{u}}^{cr} - \overset{2}{\mathbf{u}}^{cr})\,d\Gamma_{cr}}\,.
\end{aligned}
\tag{1}
$$

Here B is the complementary energy density and the superscripts m and c correspond to variables associated with the matrix and inclusion phases. $\boldsymbol{\sigma}^m$ and $\boldsymbol{\sigma}^c$ are the equilibrated stress fields, $\boldsymbol{\epsilon}^m$ and $\boldsymbol{\epsilon}^c$ the corresponding strain fields in the two phases within a Voronoi element. Also, $\mathbf{u}^e$, $\mathbf{u}^m$, $\mathbf{u}^c$, $\overset{1}{\mathbf{u}}^{cr}$ and $\overset{2}{\mathbf{u}}^{cr}$ are the kinematically admissible displacement fields on $\partial\Omega_e$,

$\partial\Omega_c^m$, $\partial\Omega_c^c$, $\overset{1}{\Gamma}_{cr}$ and $\overset{2}{\Gamma}_{cr}$, respectively. The prefix Δ corresponds to increments. The term in the first box provides the work done by the interfacial tractions $\mathbf{T}^i = T_n^i\mathbf{n}^m + T_t^i\mathbf{t}^m$ due to interfacial separation $(\mathbf{u}^m - \mathbf{u}^c)$. T_n^i and T_t^i are the normal and tangential components of interfacial traction, described by cohesive laws. The term in the second box provides the work done by the cohesive tractions $\mathbf{T}^{cr} = T_n^{cr}\mathbf{n}^{cr} + T_t^{cr}\mathbf{t}^{cr}$ due to displacement separation $(\overset{1}{\mathbf{u}}^{cr} - \overset{2}{\mathbf{u}}^{cr})$ along the crack surface, where T_n^{cr} and T_t^{cr} are the normal and tangential components of the cohesive traction. The total energy for the entire composite domain is obtained by adding the energy functionals for N elements as

$$\Pi = \sum_{e=1}^{N} \Pi_e. \tag{2}$$

2.1. Cohesive zone models for interfacial debonding and matrix cracking

Cohesive zone models, introduced in [25,26] and developed in [8,9,27–31], are effective in depicting material failure as a separation process across an extended crack tip or fracture process zone. They introduce softening in the constitutive equations, thus relating crack surface tractions to material separation across the crack. The tractions reach a maximum, subsequently decrease and eventually vanish with increasing surface separation. A wide variety of intrinsic [8,27,28,30] and extrinsic [31–33] cohesive zone models have been proposed in literature. In [34] it has been shown that the cohesive zone cannot support the hardening part with the positive slope, as in the extrinsic model, for homogeneous solids. This implies that the initial stress must be the absolute maximum as shown in Fig. 3. In cases where the cohesive zone grows along a pre-existing discontinuity, such as an interface, the cohesive region is a priori known and does not need to be constructed during simulation. In this case, the intrinsic model shown in Fig. 2 can be applied. In the following section, the two rate-independent cohesive zone models incorporated in X-VCFEM to simulate the initiation and propagation of interfacial debonding and matrix cracking, respectively, are briefly discussed.

Analogous to inter-atomic potentials in atomistic modeling, a free cohesive energy potential ϕ_{coh} is introduced such that the traction across the cohesive surface is expressed as

$$\mathbf{T}^{coh} = \frac{\partial\phi}{\partial\delta_n}\mathbf{n} + \frac{\partial\phi}{\partial\delta_t}\mathbf{t}. \tag{3}$$

Here δ_n and δ_t correspond to the normal and tangential components of the opening displacements over the cohesive surface in the $\mathbf{n}$ and $\mathbf{t}$ directions, respectively. An effective opening displacement is defined as

$$\delta = \sqrt{\delta_n^2 + \beta^2\delta_t^2}, \tag{4}$$

where β is a coupling coefficient that allows assignment of different weights to normal and tangential opening displacements.

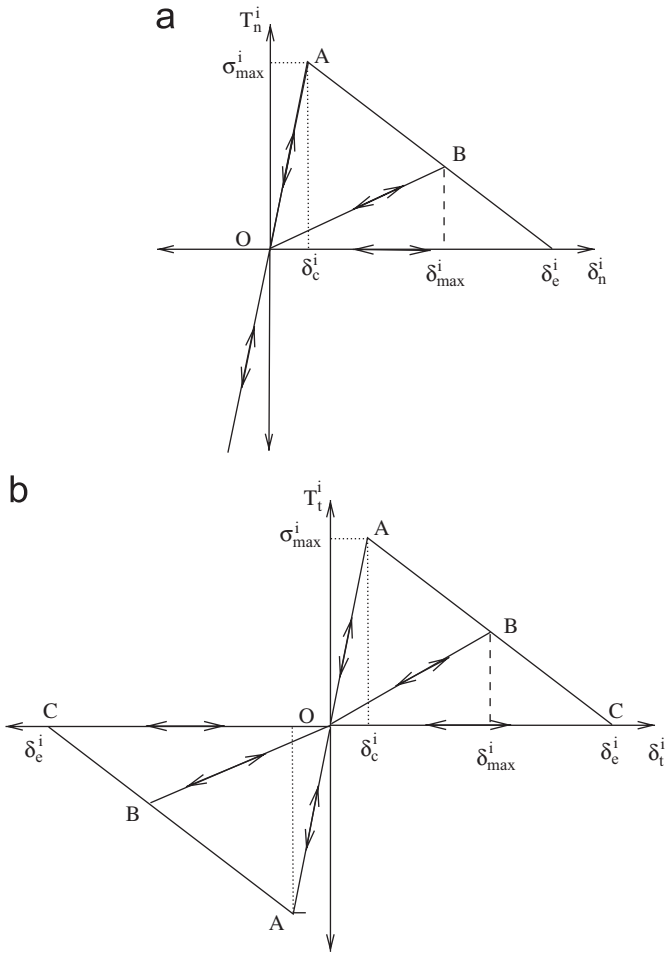

Fig. 2. (a) Normal and (b) tangential traction-displacement behavior for a bilinear cohesive zone model.

Consequently, the cohesive surface traction reduces to

$$\mathbf{T}^{coh} = \frac{t}{\delta}(\beta^2\delta_t\mathbf{t} + \delta_n\mathbf{n});$$
$$t = \frac{\partial\phi}{\partial\delta} = \sqrt{T_n^{coh^2} + \beta^{-2}T_t^{coh^2}}, \tag{5}$$

where T_n^{coh} and T_t^{coh} are the normal and tangential components of surface tractions, which can be derived as

$$T_n^{coh} = \frac{\partial\phi}{\partial\delta_n} = \frac{\partial\phi}{\partial\delta}\frac{\partial\delta}{\partial\delta_n} = t\frac{\partial\delta}{\partial\delta_n},$$
$$T_t^{coh} = \frac{\partial\phi}{\partial\delta_t} = \frac{\partial\phi}{\partial\delta}\frac{\partial\delta}{\partial\delta_t} = t\frac{\partial\delta}{\partial\delta_t}. \tag{6}$$

In the following part, T_n^{coh} and T_t^{coh} will be expressed explicitly according to the form of t. The superscripts $(\cdot)^i$ and $(\cdot)^c$ will correspond to interface debond and matrix crack, respectively.

2.1.1. Bilinear cohesive zone model for the interface debonding

The bilinear cohesive zone model, a typical three-stage intrinsic model, is used to describe the behavior of the interface

between fiber and matrix. In this model [31], t^{i} is expressed as a bilinear function of the interfacial separation as

$$t^{\mathrm{i}} = \begin{cases} \dfrac{\sigma^{\mathrm{i}}_{\max}}{\delta^{\mathrm{i}}_{\mathrm{c}}}\delta^{\mathrm{i}} & \forall\, \delta^{\mathrm{i}} < \delta^{\mathrm{i}}_{\mathrm{c}}, \\ \dfrac{\delta^{\mathrm{i}} - \delta^{\mathrm{i}}_{e}}{\delta^{\mathrm{i}}_{\mathrm{c}} - \delta^{\mathrm{i}}_{e}}\sigma^{\mathrm{i}}_{\max} & \forall\, \delta^{\mathrm{i}} \geqslant \delta^{\mathrm{i}}_{\mathrm{c}} \end{cases} \tag{7}$$

from which the normal and tangential tractions along the interface are derived as

$$T^{\mathrm{i}}_{\mathrm{n}} = \begin{cases} \dfrac{\sigma^{\mathrm{i}}_{\max}}{\delta^{\mathrm{i}}_{\mathrm{c}}}\delta^{\mathrm{i}}_{\mathrm{n}} & \text{if } \delta^{\mathrm{i}} \leqslant \delta^{\mathrm{i}}_{\mathrm{c}}, \\ \dfrac{\sigma^{\mathrm{i}}_{\max}}{\delta^{\mathrm{i}}}\dfrac{\delta^{\mathrm{i}} - \delta^{\mathrm{i}}_{e}}{\delta^{\mathrm{i}}_{\mathrm{c}} - \delta^{\mathrm{i}}_{e}}\delta^{\mathrm{i}}_{\mathrm{n}} & \text{if } \delta^{\mathrm{i}}_{\mathrm{c}} < \delta^{\mathrm{i}} \leqslant \delta^{\mathrm{i}}_{e}, \\ 0 & \text{if } \delta^{\mathrm{i}} > \delta^{\mathrm{i}}_{e}, \end{cases}$$

$$T^{\mathrm{i}}_{\mathrm{t}} = \begin{cases} \dfrac{\sigma^{\mathrm{i}}_{\max}}{\delta^{\mathrm{i}}_{\mathrm{c}}}(\beta^{\mathrm{i}})^2\delta^{\mathrm{i}}_{\mathrm{t}} & \text{if } \delta^{\mathrm{i}} < \delta^{\mathrm{i}}_{\mathrm{c}}, \\ \dfrac{\sigma^{\mathrm{i}}_{\max}}{\delta^{\mathrm{i}}}\dfrac{\delta^{\mathrm{i}} - \delta^{\mathrm{i}}_{e}}{\delta^{\mathrm{i}}_{\mathrm{c}} - \delta^{\mathrm{i}}_{e}}(\beta^{\mathrm{i}})^2\delta^{\mathrm{i}}_{\mathrm{t}} & \text{if } \delta^{\mathrm{i}}_{\mathrm{c}} < \delta^{\mathrm{i}} \leqslant \delta^{\mathrm{i}}_{e}, \\ 0 & \text{if } \delta^{\mathrm{i}} > \delta^{\mathrm{i}}_{e}. \end{cases} \tag{8}$$

Fig. 2(a,b) show the normal traction-separation response for $\delta^{\mathrm{i}}_{\mathrm{t}} = 0$ and tangential traction-separation response for $\delta^{\mathrm{i}}_{\mathrm{n}} = 0$, respectively. When the normal displacement $\delta^{\mathrm{i}}_{\mathrm{n}}$ is positive, the traction at the interface increases linearly to a maximum value of $\sigma^{\mathrm{i}}_{\max}$ (point A) corresponding to a value of $\delta^{\mathrm{i}}_{\mathrm{c}}$ before it starts decreasing to zero at a value of δ^{i}_{e} (point C). The unloading behavior in the hardening region is linear following the loading path. In the softening region, the unloading proceeds along a different linear path from the current position to the origin with a reduced stiffness. This is shown by the line BO in Fig. 2(b), for which the $t - \delta^{\mathrm{i}}$ relation is

$$t^{\mathrm{i}} = \frac{\sigma^{\mathrm{i}}_{\max}}{\delta^{\mathrm{i}}_{\max}}\frac{\delta^{\mathrm{i}}_{\max} - \delta^{\mathrm{i}}_{e}}{\delta^{\mathrm{i}}_{\mathrm{c}} - \delta^{\mathrm{i}}_{e}}\delta^{\mathrm{i}}, \quad \delta^{\mathrm{i}}_{\mathrm{c}} < \delta^{\mathrm{i}}_{\max} < \delta^{\mathrm{i}}_{e} \text{ and } \delta^{\mathrm{i}} < \delta^{\mathrm{i}}_{\max}. \tag{9}$$

Reloading follows the path OBC demonstrating the irreversible nature of the damage process. Both normal and tangential tractions vanish when $\delta^{\mathrm{i}} > \delta^{\mathrm{i}}_{e}$. The magnitudes of the tangential traction-displacement relation are independent of the sign, and hence the behavior is same for $\delta^{\mathrm{i}}_{\mathrm{t}}$ positive and negative. When the normal displacement is negative in compression, stiff penalty springs with high stiffnesses are introduced between the node-pairs at the interface. Unlike the polynomial and exponential cohesive models [8,27,31], the location of the separation at debonding point is independent of the location of the peak of the curve for the bilinear model. This gives flexibility to adjust interfacial parameters for the peak and debonding locations to match the experimental observations. The cohesive parameters in this study are calibrated from experiments done for epoxy-steel composites as discussed in [19,13].

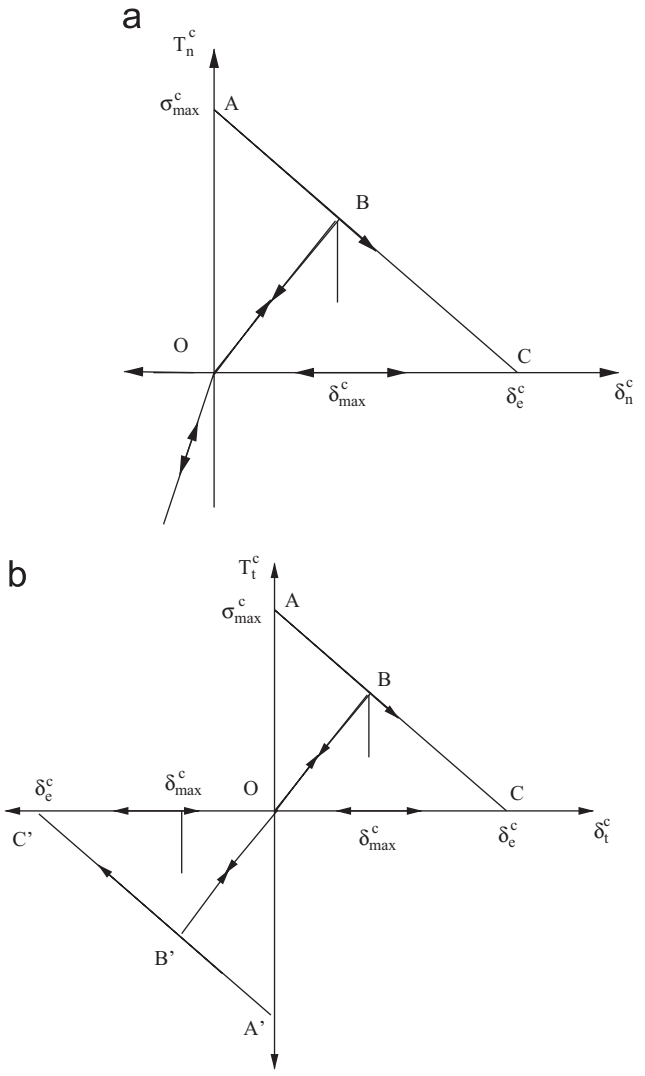

Fig. 3. Normal and tangential traction-separation behavior for the linear cohesive zone model.

2.1.2. Linear cohesive zone model for matrix cracks

The cohesive model for describing matrix cracking is a three parameter rate independent linear cohesive model, proposed in [31,32]. This is an extrinsic (two stage) model, which has an infinite stiffness or slope in the rising portion of the traction-separation law up to a peak traction value. This is followed by linear descending segment till a zero traction value is reached. The effective cohesive force t in this model for increasing δ takes the form

$$t^{\mathrm{c}} = \begin{cases} \dfrac{\sigma^{\mathrm{c}}_{\max}(\delta^{\mathrm{c}}_{e} - \delta^{\mathrm{c}})}{\delta^{\mathrm{c}}_{e}} & \forall\, \delta^{\mathrm{c}} < \delta^{\mathrm{c}}_{e}, \\ 0 & \forall\, \delta^{\mathrm{c}} \geqslant \delta^{\mathrm{c}}_{e}, \end{cases} \tag{10}$$

δ^{c}_{e} corresponds to the separation at which t^{c} goes to zero and $\sigma^{\mathrm{c}}_{\max}$ is the peak value of t^{c}. The effective normal traction-separation response of this model is depicted in Fig. 3. The normal and tangential tractions along the interface are

derived as

$$T_{\mathrm{n}}^{\mathrm{c}} = \begin{cases} \dfrac{\sigma_{\max}^{\mathrm{c}}}{\delta^{\mathrm{c}}} \dfrac{\delta_e^{\mathrm{c}} - \delta^{\mathrm{c}}}{\delta_e^{\mathrm{c}}} \delta_{\mathrm{n}}^{\mathrm{c}} & \text{if } \delta^{\mathrm{c}} \leqslant \delta_e^{\mathrm{c}}, \\ 0 & \text{if } \delta^{\mathrm{c}} > \delta_e^{\mathrm{c}}, \end{cases}$$

$$T_{\mathrm{t}}^{\mathrm{c}} = \begin{cases} \dfrac{\sigma_{\max}^{\mathrm{c}}}{\delta^{\mathrm{c}}} \dfrac{\delta_e^{\mathrm{c}} - \delta^{\mathrm{c}}}{\delta_e^{\mathrm{c}}} (\beta^{\mathrm{c}})^2 \delta_{\mathrm{t}}^{\mathrm{c}} & \text{if } \delta^{\mathrm{c}} \leqslant \delta_e^{\mathrm{c}}, \\ 0 & \text{if } \delta^{\mathrm{c}} > \delta_e^{\mathrm{c}}. \end{cases} \tag{11}$$

In the softening region, unloading from any point on the traction-separation curve proceeds along a linear path from the current position to the origin as shown by the line BO in Fig. 3. The corresponding $t - \delta^{\mathrm{c}}$ relation is

$$t^{\mathrm{c}} = \frac{\sigma_{\max}^{\mathrm{c}}}{\delta_e^{\mathrm{c}}} \frac{\delta_e^{\mathrm{c}} - \delta_{\max}^{\mathrm{c}}}{\delta_{\max}^{\mathrm{c}}} \delta^{\mathrm{c}} \quad \forall \delta^{\mathrm{c}} \leqslant \delta_{\max}^{\mathrm{c}} \leqslant \delta_e^{\mathrm{c}}. \tag{12}$$

Reloading follows the path OBC with a reduced stiffness in comparison with the original stiffness. The traction vanishes for $\delta^{\mathrm{c}} \geqslant \delta_e^{\mathrm{c}}$. For negative normal displacement (compression), stiff penalty springs with high stiffness are introduced between the node-pairs on the crack face. To define the tangent stiffness matrix, it is necessary to distinguish between crack initiation ($\delta = 0$) and crack propagation from an initialized state ($\delta > 0$). For initiation $T_{\mathrm{n}}^{\mathrm{c}} = t^{\mathrm{c}}$, and $T_{\mathrm{t}}^{\mathrm{c}} = 0$ are assumed, which imply that the initiation is in pure mode I.

2.2. General element assumptions and weak form

In the absence of body forces, two dimensional stress fields satisfying equilibrium relations can be generated from the Airy's stress function $\Phi(x, y)$. In the incremental formulation, stress increments in matrix and inclusion are obtained from derivatives of the stress functions $\Delta\Phi^{\mathrm{m}}(x, y)$ and $\Delta\Phi^{\mathrm{c}}(x, y)$ as

$$\begin{pmatrix} \Delta\sigma_{xx}^{\mathrm{m}} \\ \Delta\sigma_{yy}^{\mathrm{m}} \\ \Delta\sigma_{xy}^{\mathrm{m}} \end{pmatrix} = \begin{pmatrix} \dfrac{\partial^2 \Delta\Phi^{\mathrm{m}}}{\partial y^2} \\ \dfrac{\partial^2 \Delta\Phi^{\mathrm{m}}}{\partial x^2} \\ -\dfrac{\partial^2 \Delta\Phi^{\mathrm{m}}}{\partial x \partial y} \end{pmatrix} = [\mathbf{P}^{\mathrm{m}}(x, y)]\{\Delta\beta^{\mathrm{m}}\},$$

$$\begin{pmatrix} \Delta\sigma_{xx}^{\mathrm{c}} \\ \Delta\sigma_{yy}^{\mathrm{c}} \\ \Delta\sigma_{xy}^{\mathrm{c}} \end{pmatrix} = \begin{pmatrix} \dfrac{\partial^2 \Delta\Phi^{\mathrm{c}}}{\partial y^2} \\ \dfrac{\partial^2 \Delta\Phi^{\mathrm{c}}}{\partial x^2} \\ -\dfrac{\partial^2 \Delta\Phi^{\mathrm{c}}}{\partial x \partial y} \end{pmatrix} = [\mathbf{P}^{\mathrm{c}}(x, y)]\{\Delta\beta^{\mathrm{c}}\}, \tag{13}$$

where $\{\Delta\beta^{\mathrm{m}}\}$ and $\{\Delta\beta^{\mathrm{c}}\}$ are the column of unknown stress increment coefficients. Convergence properties and efficiency of X-VCFEM depend on the choice of Φ^{m}. These functions should adequately account for the geometry and location of the heterogeneity in the element, so stress functions for matrix are decomposed into (a) a purely polynomial function $\mathbf{\Phi}_{\mathrm{poly}}^{\mathrm{m}}$, (b) a reciprocal function $\mathbf{\Phi}_{\mathrm{rec}}^{\mathrm{m}}$, (c) a branch function $\mathbf{\Phi}_{\mathrm{branch}}^{\mathrm{m}}$ and (d) wavelet functions $\mathbf{\Phi}_{\mathrm{wvlt}}^{\mathrm{m}}$ ($\mathbf{\Phi}^{\mathrm{m}} = \mathbf{\Phi}_{\mathrm{poly}}^{\mathrm{m}} + \mathbf{\Phi}_{\mathrm{rec}}^{\mathrm{m}} + \mathbf{\Phi}_{\mathrm{branch}}^{\mathrm{m}} + \mathbf{\Phi}_{\mathrm{wvlt}}^{\mathrm{m}}$). The selection of stress functions are discussed in [20,14] with details. Inclusion stress functions are admitted as polynomial function $\mathbf{\Phi}_{\mathrm{poly}}^{\mathrm{c}}$ ($\mathbf{\Phi}^{\mathrm{c}} = \mathbf{\Phi}_{\mathrm{poly}}^{\mathrm{c}}$). Compatible displacement fields satisfying inter-element continuity on the element boundary $\partial\Omega_e$ and intra-element continuity on both the interface $\partial\Omega_{\mathrm{c}}^{\mathrm{m}}/\partial\Omega_{\mathrm{c}}^{\mathrm{c}}$ and the crack face Γ_{cr} are generated by interpolation of nodal displacements as

$$\{\Delta\mathbf{u}^e\} = [\mathbf{L}^e]\{\Delta\mathbf{q}^e\} \text{ on } \partial\Omega_e, \quad \{\Delta\mathbf{u}^{\mathrm{m}}\} = [\mathbf{L}^{\mathrm{m}}]\{\Delta\mathbf{q}^{\mathrm{m}}\} \text{ on } \partial\Omega_{\mathrm{c}}^{\mathrm{m}},$$

$$\{\Delta\mathbf{u}^{\mathrm{c}}\} = [\mathbf{L}^{\mathrm{c}}]\{\Delta\mathbf{q}^{\mathrm{c}}\} \text{ on } \partial\Omega_{\mathrm{c}}^{\mathrm{c}}, \quad \{\Delta\overset{1}{\mathbf{u}}^{\mathrm{cr}}\} = [\overset{1}{\mathbf{L}}^{\mathrm{cr}}]\{\Delta\overset{1}{\mathbf{q}}^{\mathrm{cr}}\} \text{ on } \overset{1}{\Gamma}_{\mathrm{cr}},$$

$$\{\Delta\overset{2}{\mathbf{u}}^{\mathrm{cr}}\} = [\overset{2}{\mathbf{L}}^{\mathrm{cr}}]\{\Delta\overset{2}{\mathbf{q}}^{\mathrm{cr}}\} \text{ on } \overset{2}{\Gamma}_{\mathrm{cr}}. \tag{14}$$

The interpolation matrices $[\mathbf{L}^e]$, $[\mathbf{L}^{\mathrm{m}}]$, $[\mathbf{L}^{\mathrm{c}}]$, $[\overset{1}{\mathbf{L}}^{\mathrm{cr}}]$, $[\overset{2}{\mathbf{L}}^{\mathrm{cr}}]$ for the nodal displacements on the respective boundaries are constructed using standard linear or hierarchical shape functions. Since nodes on the interface and crack surfaces are always belonging to some node-pair, the interpolation matrices are chosen as $[\mathbf{L}^{\mathrm{m}}] = [\mathbf{L}^{\mathrm{c}}]$ and $[\overset{1}{\mathbf{L}}^{\mathrm{cr}}] = [\overset{2}{\mathbf{L}}^{\mathrm{cr}}]$. Substituting the interpolations of stress and displacement fields from Eqs. (13) and (14) into Eq. (1) results in the matrix form of the element complimentary energy

$$\begin{aligned} \Pi_e = & -\frac{1}{2}\{\boldsymbol{\beta}^{\mathbf{m}} + \Delta\boldsymbol{\beta}^{\mathbf{m}}\}^{\mathrm{T}}[\mathbf{H}^{\mathrm{m}}]\{\boldsymbol{\beta}^{\mathbf{m}} + \Delta\boldsymbol{\beta}^{\mathbf{m}}\} \\ & -\frac{1}{2}\{\boldsymbol{\beta}^{\mathbf{c}} + \Delta\boldsymbol{\beta}^{\mathbf{c}}\}^{\mathrm{T}}[\mathbf{H}^{\mathrm{c}}]\{\boldsymbol{\beta}^{\mathbf{c}} + \Delta\boldsymbol{\beta}^{\mathbf{c}}\} \\ & + \{\boldsymbol{\beta}^{\mathbf{m}} + \Delta\boldsymbol{\beta}^{\mathbf{m}}\}^{\mathrm{T}}[\mathbf{G}]^e\{\mathbf{q}^e + \Delta\mathbf{q}^e\} \\ & - \{\boldsymbol{\beta}^{\mathbf{m}} + \Delta\boldsymbol{\beta}^{\mathbf{m}}\}^{\mathrm{T}}[\mathbf{G}]^{\mathrm{m}}\{\mathbf{q}^{\mathrm{m}} + \Delta\mathbf{q}^{\mathrm{m}}\} \\ & + \{\boldsymbol{\beta}^{\mathbf{c}} + \Delta\boldsymbol{\beta}^{\mathbf{c}}\}^{\mathrm{T}}[\mathbf{G}]^{\mathrm{c}}\{\mathbf{q}^{\mathrm{c}} + \Delta\mathbf{q}^{\mathrm{c}}\} \\ & + \{\boldsymbol{\beta}^{\mathbf{m}} + \Delta\boldsymbol{\beta}^{\mathbf{m}}\}^{\mathrm{T}}[\overset{1}{\mathbf{G}}^{\mathrm{cr}}]\{\overset{1}{\mathbf{q}}^{\mathrm{cr}} + \Delta\overset{1}{\mathbf{q}}^{\mathrm{cr}}\} \\ & - \{\boldsymbol{\beta}^{\mathbf{m}} + \Delta\boldsymbol{\beta}^{\mathbf{m}}\}^{\mathrm{T}}[\overset{2}{\mathbf{G}}^{\mathrm{cr}}]\{\overset{2}{\mathbf{q}}^{\mathrm{cr}} + \Delta\overset{2}{\mathbf{q}}^{\mathrm{cr}}\} - \{\hat{\mathbf{t}}\}^{\mathrm{T}}\{\mathbf{q}^e + \Delta\mathbf{q}^e\} \\ & - \boxed{\int_{\Gamma_{\mathrm{intf}}} \int_{(\mathbf{u}^{\mathrm{m}} - \mathbf{u}^{\mathrm{c}})}^{(\mathbf{u}^{\mathrm{m}} + \Delta\mathbf{u}^{\mathrm{m}} - \mathbf{u}^{\mathrm{c}} - \Delta\mathbf{u}^{\mathrm{c}})} \mathbf{T}^{\mathrm{i}} \cdot \mathrm{d}(\mathbf{u}^{\mathrm{m}} - \mathbf{u}^{\mathrm{c}})\, \mathrm{d}\partial\Omega} \\ & - \boxed{\int_{\Gamma_{\mathrm{cr}}} \int_{\overset{1}{\mathbf{u}}^{\mathrm{cr}} - \overset{2}{\mathbf{u}}^{\mathrm{cr}}}^{\overset{1}{\mathbf{u}}^{\mathrm{cr}} + \Delta\overset{1}{\mathbf{u}}^{\mathrm{cr}} - \overset{2}{\mathbf{u}}^{\mathrm{cr}} - \Delta\overset{2}{\mathbf{u}}^{\mathrm{cr}}} \mathbf{T}^{\mathrm{cr}} \cdot \mathrm{d}(\overset{1}{\mathbf{u}}^{\mathrm{cr}} - \overset{2}{\mathbf{u}}^{\mathrm{cr}})\, \mathrm{d}\Gamma_{\mathrm{cr}}}, \end{aligned} \tag{15}$$

where

$$[\mathbf{H}^{\mathrm{m}}] = \int_{\Omega_e} [\mathbf{P}^{\mathrm{m}}]^{\mathrm{T}}[\mathbf{S}^{\mathrm{m}}][\mathbf{P}^{\mathrm{m}}]\, \mathrm{d}\Omega_{\mathrm{m}},$$

$$[\mathbf{H}^{\mathrm{c}}] = \int_{\Omega_e} [\mathbf{P}^{\mathrm{c}}]^{\mathrm{T}}[\mathbf{S}^{\mathrm{c}}][\mathbf{P}^{\mathrm{c}}]\, \mathrm{d}\Omega_{\mathrm{c}},$$

$$[\mathbf{G}^e] = \int_{\partial\Omega_e} [\mathbf{P}^{\mathrm{m}}]^{\mathrm{T}}[\mathbf{n}^e][\mathbf{L}^e]\, \mathrm{d}\partial\Omega_{\mathrm{m}},$$

$$[\mathbf{G}^{\mathrm{m}}] = \int_{\partial\Omega_e} [\mathbf{P}^{\mathrm{m}}]^{\mathrm{T}}[\mathbf{n}^{\mathrm{m}}][\mathbf{L}^{\mathrm{m}}]\, \mathrm{d}\partial\Omega_{\mathrm{m}},$$

$$[\mathbf{G}^{\mathrm{c}}] = \int_{\partial\Omega_e} [\mathbf{P}^{\mathrm{c}}]^{\mathrm{T}} [\mathbf{n}^{\mathrm{c}}] [\mathbf{L}^{\mathrm{c}}] \, \mathrm{d}\partial\Omega_{\mathrm{c}},$$

$$[\overset{1}{\mathbf{G}}{}^{\mathrm{cr}}] = \int_{\overset{1}{\Gamma}_{\mathrm{cr}}} [\mathbf{P}^{\mathrm{m}}]^{\mathrm{T}} [\mathbf{n}^{\mathrm{cr}}] [\overset{1}{\mathbf{L}}_{\mathrm{cr}}] \, \mathrm{d}\Gamma_{\mathrm{cr}},$$

$$[\overset{2}{\mathbf{G}}{}^{\mathrm{cr}}] = \int_{\overset{2}{\Gamma}_{\mathrm{cr}}} [\mathbf{P}^{\mathrm{m}}]^{\mathrm{T}} [\mathbf{n}^{\mathrm{cr}}] [\overset{2}{\mathbf{L}}_{\mathrm{cr}}] \, \mathrm{d}\Gamma_{\mathrm{cr}},$$

$$\{\hat{\mathbf{t}}\} = \int_{\Gamma_{\mathrm{tm}}} [\mathbf{L}_e]^{\mathrm{T}} \{\bar{\mathbf{t}} + \Delta\bar{\mathbf{t}}\} \, \mathrm{d}\Gamma_{\mathrm{tm}}. \tag{16}$$

The terms in the first and second boxes of Eq. (15) express the cohesive energy of the interface and crack deformation, respectively. Construction of appropriate stress functions with optimally high resolution is necessary for accurately depicting high stress gradients near the crack tip.

2.3. Solution method

Crack growth in multiply cracked materials is solved using an incremental approach, where a set of elemental and global equations are solved in each increment for stresses and displacements.

1. Local equations for each element are obtained by setting the variation of Eq. (15) with respect to the stress coefficients $\Delta\boldsymbol{\beta}^{\mathbf{m}}$ and $\Delta\boldsymbol{\beta}^{\mathbf{c}}$ to zero. This results in the weak form of the element kinematic relations

$$\begin{bmatrix} [\mathbf{H}^{\mathrm{m}}] & [\mathbf{0}] \\ [\mathbf{0}] & [\mathbf{H}^{\mathrm{c}}] \end{bmatrix} \begin{Bmatrix} \boldsymbol{\beta}^{\mathrm{m}} + \Delta\boldsymbol{\beta}^{\mathrm{m}} \\ \boldsymbol{\beta}^{\mathrm{c}} + \Delta\boldsymbol{\beta}^{\mathrm{c}} \end{Bmatrix} = \begin{bmatrix} [\mathbf{G}^e] & -[\mathbf{G}^{\mathrm{m}}] & [\mathbf{0}] & [\overset{1}{\mathbf{G}}{}^{\mathrm{cr}}] & -[\overset{2}{\mathbf{G}}{}^{\mathrm{cr}}] \\ [\mathbf{0}] & [\mathbf{0}] & [\mathbf{G}^{\mathrm{c}}] & [\mathbf{0}] & [\mathbf{0}] \end{bmatrix} \times \begin{Bmatrix} \mathbf{q}^e + \Delta\mathbf{q}^e \\ \mathbf{q}^{\mathrm{m}} + \Delta\mathbf{q}^{\mathrm{m}} \\ \mathbf{q}^{\mathrm{c}} + \Delta\mathbf{q}^{\mathrm{c}} \\ \overset{1}{\mathbf{q}}{}^{\mathrm{cr}} + \Delta\overset{1}{\mathbf{q}}{}^{\mathrm{cr}} \\ \overset{2}{\mathbf{q}}{}^{\mathrm{cr}} + \Delta\overset{2}{\mathbf{q}}{}^{\mathrm{cr}} \end{Bmatrix} \tag{17}$$

or in a condensed form

$$[\mathbf{H}]_e \{\boldsymbol{\beta} + \Delta\boldsymbol{\beta}\}_e = [\mathbf{G}]_e \{\mathbf{q} + \Delta\mathbf{q}\}_e. \tag{18}$$

Since Eq. (18) is linear, the stress coefficients can be directly expressed in terms of the nodal displacements, provided the element $[\mathbf{H}]_e$ matrix is invertible.

2. Subsequently, the weak forms of the global traction continuity conditions are solved by setting the variation of the total domain energy functional with respect to the generalized displacement components to zero. This results in the weak form of the traction reciprocity conditions

$$\sum_{e=1}^{N} \begin{bmatrix} [\mathbf{G}^e] & -[\mathbf{G}^{\mathrm{m}}] & [\mathbf{0}] & [\overset{1}{\mathbf{G}}{}^{\mathrm{cr}}] & -[\overset{2}{\mathbf{G}}{}^{\mathrm{cr}}] \\ [\mathbf{0}] & [\mathbf{0}] & [\mathbf{G}^{\mathrm{c}}] & [\mathbf{0}] & [\mathbf{0}] \end{bmatrix}_e^{\mathrm{T}} \times \begin{Bmatrix} \boldsymbol{\beta}^{\mathbf{m}} + \Delta\boldsymbol{\beta}^{\mathbf{m}} \\ \boldsymbol{\beta}^{\mathbf{c}} + \Delta\boldsymbol{\beta}^{\mathbf{c}} \end{Bmatrix}_e = \sum_{e=1}^{N} \begin{Bmatrix} \hat{\mathbf{t}} \\ \bar{\mathbf{f}}_{\mathrm{coh}}^{\mathrm{in}} \\ -\bar{\mathbf{f}}_{\mathrm{coh}}^{\mathrm{in}} \\ \bar{\mathbf{f}}_{\mathrm{coh}}^{\mathrm{cr}} \\ -\bar{\mathbf{f}}_{\mathrm{coh}}^{\mathrm{cr}} \end{Bmatrix}_e \tag{19}$$

or in a condensed form

$$\sum_{e=1}^{N} [\mathbf{G}]_e^{\mathrm{T}} \{\boldsymbol{\beta} + \Delta\boldsymbol{\beta}\}_e = \sum_{e=1}^{N} \{\bar{\mathbf{T}}_{\mathrm{ext}}\}_e. \tag{20}$$

The forces at the matrix-inclusion interface and the matrix crack surface are, respectively, expressed in terms of the cohesive energy as

$$\bar{\mathbf{f}}_{\mathrm{coh}}^{\mathrm{m}} = \int_{\Gamma_{\mathrm{intf}}} \frac{\partial[\int_{(\mathbf{u}^{\mathrm{m}}-\mathbf{u}^{\mathrm{c}})}^{(\mathbf{u}^{\mathrm{m}}+\Delta\mathbf{u}^{\mathrm{m}}-\mathbf{u}^{\mathrm{c}}-\Delta\mathbf{u}^{\mathrm{c}})} \mathbf{T}^{\mathrm{i}} \cdot \mathrm{d}(\mathbf{u}^{\mathrm{m}} - \mathbf{u}^{\mathrm{c}})]}{\partial\Delta\mathbf{q}^{\mathrm{m}}} \, \mathrm{d}\partial\Omega = \int_{\Gamma_{\mathrm{intf}}} [\mathbf{L}^{\mathrm{m}}]^{\mathrm{T}} \{\mathbf{T}^{\mathrm{i}}(\mathbf{u}^{\mathrm{m}} + \Delta\mathbf{u}^{\mathrm{m}} - \mathbf{u}^{\mathrm{c}} - \Delta\mathbf{u}^{\mathrm{c}})\} \, \mathrm{d}\partial\Omega \tag{21}$$

and

$$\bar{\mathbf{f}}_{\mathrm{coh}}^{\mathrm{cr}} = \int_{\Gamma_{\mathrm{cr}}} \frac{\partial \left[\int_{\overset{1}{\mathbf{u}}{}^{\mathrm{cr}}-\overset{2}{\mathbf{u}}{}^{\mathrm{cr}}}^{\overset{1}{\mathbf{u}}{}^{\mathrm{cr}}+\Delta\overset{1}{\mathbf{u}}{}^{\mathrm{cr}}-\overset{2}{\mathbf{u}}{}^{\mathrm{cr}}-\Delta\overset{2}{\mathbf{u}}{}^{\mathrm{cr}}} \mathbf{T}^{\mathrm{cr}} \cdot \mathrm{d}(\overset{1}{\mathbf{u}}{}^{\mathrm{cr}} - \overset{2}{\mathbf{u}}{}^{\mathrm{cr}}) \right]}{\partial\Delta\,\overset{1}{\mathbf{q}}{}^{\mathrm{cr}}} \, \mathrm{d}\Gamma_{\mathrm{cr}} = \int_{\Gamma_{\mathrm{cr}}} [\overset{1}{\mathbf{L}}{}^{\mathrm{cr}}]^{\mathrm{T}} \{\mathbf{T}^{\mathrm{cr}}(\overset{1}{\mathbf{u}}{}^{\mathrm{cr}} + \Delta\overset{1}{\mathbf{u}}{}^{\mathrm{cr}} - \overset{2}{\mathbf{u}}{}^{\mathrm{cr}} - \Delta\overset{2}{\mathbf{u}}{}^{\mathrm{cr}})\} \, \mathrm{d}\Gamma_{\mathrm{cr}}. \tag{22}$$

Combining Eqs. (18) and (20) and eliminating the stress coefficients $\{\boldsymbol{\beta} + \Delta\boldsymbol{\beta}\}_e$, results in the equation for solving the generalized displacements as

$$\sum_{e=1}^{N} \{[\mathbf{G}]_e^{\mathrm{T}} [\mathbf{H}]_e^{-1} [\mathbf{G}]_e\} \{\mathbf{q} + \Delta\mathbf{q}\} = \sum_{e=1}^{N} \{\bar{\mathbf{T}}_{\mathrm{ext}}\}_e. \tag{23}$$

Eq. (23) is a nonlinear matrix equation system due to the cohesive laws. Consequently, a Newton–Raphson iterative solver is invoked to solve for the increments of nodal displacements. The linearized form of Eq. (23) for the jth iteration is

$$\left\{ \sum_{e=1}^{N} \frac{\partial\{\bar{\mathbf{T}}_{\mathrm{ext}}\}_e}{\partial\{\mathbf{q}\}} - \sum_{e=1}^{N} \{[\mathbf{G}]^{\mathrm{T}} [\mathbf{H}]^{-1} [\mathbf{G}]\}_e \right\}^j \{\mathrm{d}\mathbf{q}\}^j = \left\{ \sum_{e=1}^{N} \{\bar{\mathbf{T}}_{\mathrm{ext}}\}_e - \sum_{e=1}^{N} \{[\mathbf{G}]^{\mathrm{T}} [\mathbf{H}]^{-1} [\mathbf{G}]\}_e \{\mathbf{q} + \Delta\mathbf{q}\} \right\}^j \tag{24}$$

which, in a condensed form is

$$[\mathbf{K}^{\mathrm{g}}]^j \, \mathrm{d}\mathbf{q}^j = \{\mathbf{R}_{\mathrm{ext}}^{\mathrm{g}}\} - \{\mathbf{R}_{\mathrm{int}}^{\mathrm{g}}\}^j. \tag{25}$$

Many numerical examples in the literature have shown that only a Newton-Raphson iterative solver cannot obtain the entire failure solution for problems involving damage, especially when snap-back appears in the load-deformation curve. To account for this, the arc-length method proposed in [35–37] is introduced in X-VCFEM. In this method, an unknown loading parameter $(\lambda + \mathrm{d}\lambda)$ governs the load increments through a modification in Eq. (25) as

$$[\mathbf{K}^{\mathrm{g}}]^j \, \mathrm{d}\mathbf{q}^j = (\lambda^j + \mathrm{d}\lambda^j)\{\mathbf{R}^{\mathrm{g}}_{\mathrm{ext}}\} - \{\mathbf{R}^{\mathrm{g}}_{\mathrm{int}}\}^j, \tag{26}$$

where both $\mathrm{d}\lambda^j$ and $\mathrm{d}\mathbf{q}^j$ are unknowns and $\mathrm{d}\lambda^j$ can be either positive or negative. The additional unknown $\mathrm{d}\lambda^j$ requires the solution of a constraint equation, written in terms of the magnitude of the deformation of all the nodes on the crack surface as

$$\sum_{i \in \mathrm{Coh}} (\Delta \mathbf{u}_i)^2 = \Delta l^2, \tag{27}$$

where $i \in \mathrm{Coh}$ represents the set of all nodes on both the crack surfaces and fiber-matrix interfaces.

3. Numerical implementation

3.1. Adaptive criteria for determining the direction and length of the incremental crack advance

Criteria based on the cohesive energy at the damage onset point have been introduced in [20,38] to determine the direction and length of the incremental cohesive crack. The angle representing direction of the incremental matrix crack advance α_{c} is obtained at a crack tip as

$$\alpha_{\mathrm{c}} = \begin{cases} \arctan\left(\dfrac{-\sigma_{xx}+\sigma_{yy} \pm \sqrt{(\sigma_{xx}-\sigma_{yy})^2+4\sigma_{xy}^2}}{2\sigma_{xy}}\right), \\ \arctan\left(\dfrac{2(\beta^{\mathrm{m}2}-1)\sigma_{xy} \pm \sqrt{(4\beta^{\mathrm{m}4}-8\beta^{\mathrm{m}2}+4)\sigma_{xy}^2-(4\beta^{\mathrm{m}4}-4\beta^{\mathrm{m}2}+2)\sigma_{xx}\sigma_{yy}-(2\beta^{\mathrm{m}2}-1)(\sigma_{xx}^2+\sigma_{yy}^2)}}{2\beta^{\mathrm{m}2}\sigma_{xx}-\sigma_{xx}+\sigma_{yy}}\right). \end{cases} \tag{28}$$

The sign in Eq. (28) is chosen as the one that maximizes the cohesive energy ϕ_{c}. Upon establishing the direction of incremental cohesive crack growth α_{c}, the incremental length of cohesive zone advance $(\Delta\bar{l})$ is estimated as

$$\Delta\bar{l} = \frac{\phi_A}{\phi_A - \phi_B}|AB|. \tag{29}$$

Here **A** is the damage onset point on the interface and **B** is a point close to **A** in the direction of crack propagation.

3.2. Adaptive criterion for the cohesive crack branching from the interface into the matrix

Crack deflection behavior at an interface has been the subject of various research efforts and many significant results for have been obtained in [21–24]. These studies have identified fracture toughness ratio of the interface to the matrix material as the most important parameter governing the crack branching phenomenon. Predicting crack growth requires calculation of the energy release rate G and the surface fracture energy

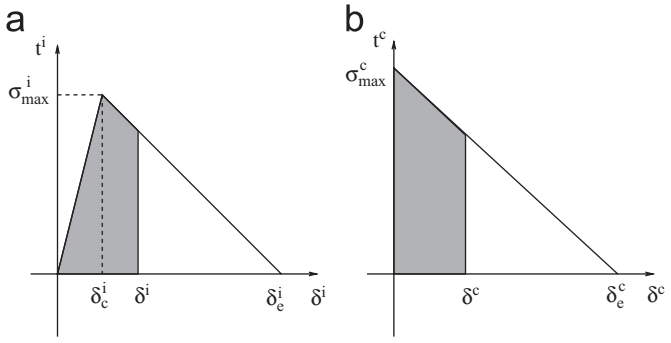

Fig. 4. Cohesive zone models for calculating energy release rates: (a) the bilinear law for interface debonding and (b) the linear law for matrix cracking.

G_{c}. The energy release rate and the critical energy release rate for crack growth along the interface are denoted by G^{i} and $G^{\mathrm{i}}_{\mathrm{c}}$, and the corresponding variables in the pure matrix phase are denoted by G^{m} and $G^{\mathrm{m}}_{\mathrm{c}}$. As shown in [13,14,19], damage at the interface results in larger stress concentration in the matrix. Once the stress in matrix reaches a critical state, the crack may bifurcate into the matrix and continue to propagate in the matrix phase.

To establish a criterion for interfacial debond deflection into the matrix, a criterion proposed by Hutchinson and He [22,23] is used. This criterion is based on the relative energy release rates in the interface and the matrix using formulae in linear elastic fracture mechanics or LEFM. The crack branching occurs when the ratio of the energy release rate to a critical energy release rate in the matrix exceeds the corresponding ratio at the interface, i.e.

$$\frac{G^{\mathrm{m}}}{G^{\mathrm{m}}_{\mathrm{c}}} > \frac{G^{\mathrm{i}}}{G^{\mathrm{i}}_{\mathrm{c}}}, \tag{30}$$

where G^{m}, G^{i}, $G^{\mathrm{m}}_{\mathrm{c}}$, $G^{\mathrm{i}}_{\mathrm{c}}$ are the current and critical energy release rates in the matrix and interface, respectively. The cohesive energy has been shown to be equivalent to the energy release rate in [31] and hence cohesive energies are used in Eq. (30). Schematics of the calculation of energy release rates for the cohesive zone model are shown in Fig. 4(a) for damage at the interface, and in Fig. 4(b) for matrix cracking. The area under the shadowed regions correspond to the released cohesive energies G^{i} and G^{m}. The critical release rates for interface and matrix are, respectively, given as

$$G^{\mathrm{i}}_{\mathrm{c}} = \tfrac{1}{2}\sigma^{\mathrm{i}}_{\max}\delta^{\mathrm{i}}_{e} \quad \text{and} \quad G^{\mathrm{m}}_{\mathrm{c}} = \tfrac{1}{2}\sigma^{\mathrm{m}}_{\max}\delta^{\mathrm{m}}_{e}. \tag{31}$$

In X-VCFEM, candidate positions are chosen adaptively by evaluating the criterion (30) at 30 equidistant points between

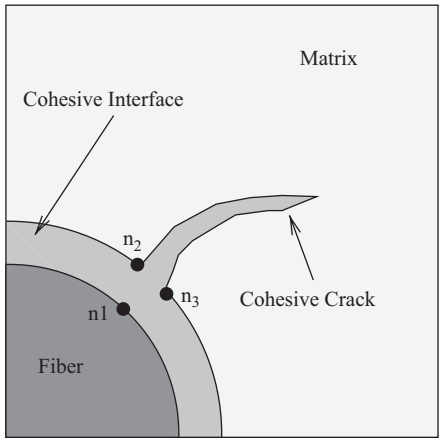

Fig. 5. Node joint (n_1, n_2, n_3) for describing the damage advance into matrix from interface.

any two consecutive nodes on the interface. To obtain G^{m}, the effective cohesive traction t is calculated from stresses (σ_{xx}, σ_{yy} and σ_{xy}) at each candidate point. Similar to the equations introduced in [20,38], the effective cohesive traction $t(\alpha_{\mathrm{c}})$, the released cohesive energy $\phi(\alpha_{\mathrm{c}})$ and the energy release rate G^{m} are obtained as

$$t(\alpha) = \sqrt{(\sigma_{xx}\sin^2\alpha - \sigma_{xy}\sin 2\alpha + \sigma_{yy}\cos^2\alpha)^2 + \beta^{-2}(-\tfrac{1}{2}\sigma_{xx}\sin 2\alpha + \sigma_{xy}\cos 2\alpha + \frac{1}{2}\sigma_{yy}\sin 2\alpha)^2}, \qquad (32)$$

$$G^{\mathrm{m}}(\alpha) = \phi(\alpha) = \frac{\delta_e^{\mathrm{m}}}{2\sigma_{\max}^{\mathrm{m}}}({\sigma_{\max}^{\mathrm{m}}}^2 - t(\alpha)^2). \qquad (33)$$

It is important to note that the value of G^{m} will depend on the direction that the candidate crack may take once it moves into the matrix. The direction of this incremental cohesive crack corresponds to an angle α_{c} that maximizes the total cohesive energy. The current energy release rates for interface is given as

$$G^{\mathrm{i}} = \begin{cases} \sigma_{\max}^{\mathrm{i}}\delta^{\mathrm{i}}/\delta_{\mathrm{c}}, & \delta < \delta_{\mathrm{c}}, \\ \dfrac{\sigma_{\max}^{\mathrm{i}}}{2}\left(\delta_e^{\mathrm{i}} - \dfrac{(\delta_e^{\mathrm{i}} - \delta)^2}{\delta_e^{\mathrm{i}} - \delta_{\mathrm{c}}}\right), & \delta \geqslant \delta_{\mathrm{c}}. \end{cases} \qquad (34)$$

The crack branching condition (30) is calculated using Eqs. (31), (33) and (34) at candidate points on the interface, and the next increment of crack segment is decided accordingly.

Fig. 5 shows a schematic representation of the VC element after the crack has branched off into matrix. At the onset of branching off into the matrix, the matrix side of the interface is broken into two segments that belong to opposite sides of the cohesive crack. The cohesive model is introduced by a node-pair (n_2, n_3). It is important to note that along with the matrix crack, the debond can simultaneously advance along the interface. In order to describe the damage propagation along the interface, the node n_1 is added at the corresponding position on the fiber side. All node-pairs at the junction (n_1, n_2, n_3) have cohesive springs between them. This enables the VC element to predict the crack growth along both the interface and in the matrix. For each node-pair at the node junction, contributions of integrals from the interface as well as the matrix crack are summed.

4. Model validation for the two damage modes

4.1. Interfacial debonding in one fiber case

In the first example, X-VCFEM predictions are compared with experiments on debonding of composites that have been described in [13]. The experiment simulated here is conducted with a single specimens in the form of a cruciform as shown in Fig. 6(a). The cruciform shape has been developed to avoid stress singularity at the intersection of fiber-matrix interface and free surface, which occur in uniform width specimens. The onset of fiber-matrix debonding is identified with a sharp change in the slope of the experimental stress–strain curve in Fig. 6(b). Subsequent loading proceeds with a lower stress–strain slope, due to a reduced load carrying capability of the partially debonded fiber. Following failure, the specimens are sectioned at the center and fluorescent dye penetration is used to determine the total angle of debond as approximately 85° as shown in Fig. 6(c). The cohesive zone parameters have been determined in [13] by solving an inverse problem in which the difference between the experimental and simulated results is minimized. For the bilinear model the cohesive parameters are $\sigma_{\max}^{\mathrm{i}} = 0.0037\,\mathrm{GPa}$, $\delta_{\mathrm{c}}^{\mathrm{i}} = 0.0028$, $\delta_e^{\mathrm{i}} = 0.0035$, and $\beta^{\mathrm{i}} = 0.707$. The geometric properties of the composite simulated include a $6.82\,\mathrm{mm} \times 6.0\,\mathrm{mm}$ domain with a circular fiber of radius 1.18 mm. The material properties are $E_{\mathrm{steel}} = 210\,\mathrm{GPa}$, $\nu_{\mathrm{steel}} = 0.3$, $E_{\mathrm{epoxy}} = 4.6\,\mathrm{GPa}$ and $\nu_{\mathrm{epoxy}} = 0.4$. The macroscopic stress–strain plot of the simulation in Fig. 6(b), match the experimental result very well. Furthermore, the simulated debonding angle in the composite microstructure is obtained to be 90° as shown in Fig. 6(d). Both macroscopic and microscopic results obtained from X-VCFEM simulations are found to yield satisfactory comparison with experiments.

4.2. Matrix crack propagation for the bending beam

This example shows a mixed-mode cohesive crack propagation in a three-point bend test due to an unsymmetrically positioned initial crack. The problem, shown in Fig. 7(a), has been solved by Mariani and Perego [24] using XFEM under plane stress conditions. The initial crack position is determined by the offset ratio α, defined as the ratio of the distance of the initial crack from the mid-span cross-section to half of the beam span. The material Young's modulus $E = 31370\,\mathrm{MPa}$ and Poisson ratio $\nu = 0.2$. The cohesive model parameters are $\sigma_{\max}^{\mathrm{c}} = 4.4\,\mathrm{MPa}$, $\delta_e^{\mathrm{c}} = 0.07719298\,\mathrm{mm}$ and $\beta^{\mathrm{c}} = 1.0$. The entire domain is represented by a *single element* in X-VCEFM with 154 nodal degrees of freedom. The path of crack propagation is shown in Fig. 7(b). The cracks move towards the point of applied load and align itself perpendicular to the edge of the

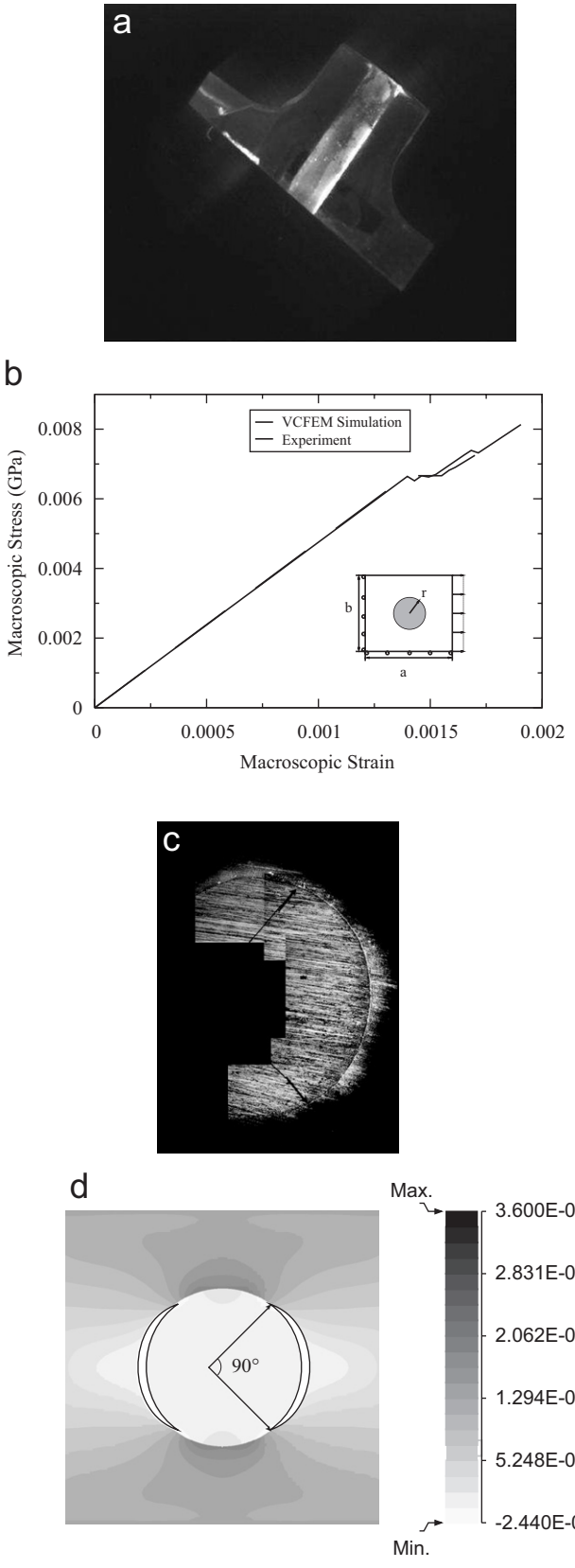

Fig. 6. Comparison of simulation with experiment: (a) faceview of the debonded cruciform specimen showing dye penetration, (b) comparison of macroscopic stress–strain response, (c) cross section indicating debonding angle as the limits of the dye penetrated region, and (d) contour plot of the microscopic stress (GPa).

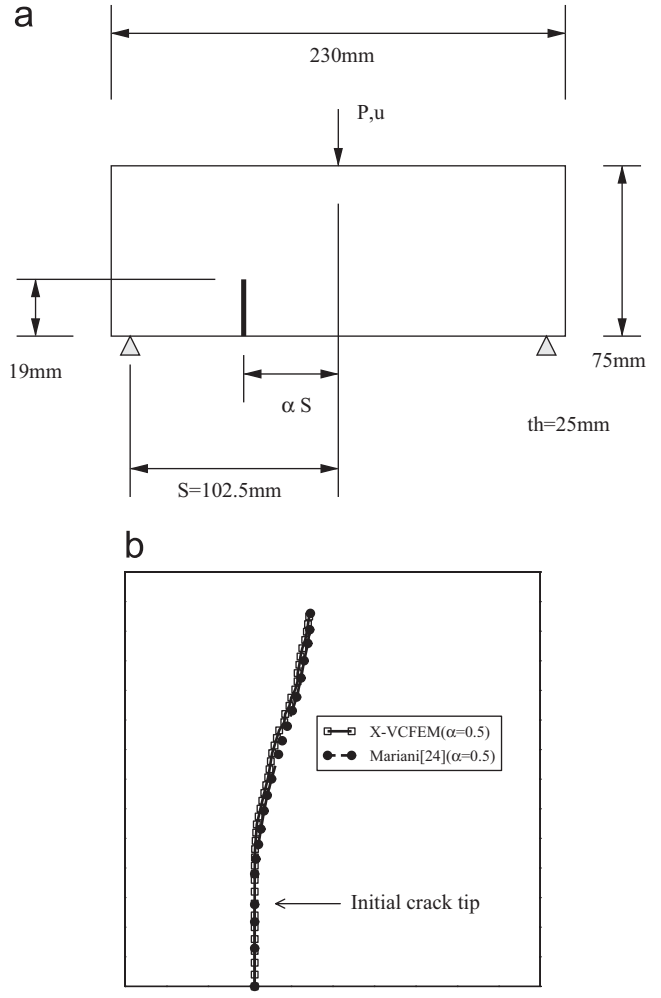

Fig. 7. (a) A three-point bending specimen with an unsymmetric initial crack and (b) comparison of the crack paths by X-VCFEM with that in [39] for $\alpha = 0.5$.

specimen. Excellent agreement is obtained between the results by X-VCFEM and in [39].

5. Numerical examples with the model including interfacial debinding and matrix cracking

Several examples with microstructures containing circular and elliptic fibers are considered to check the effectiveness of X-VCFEM. These examples also show the effect of fiber size and shape on the damage propagation with the interaction between the interface and matrix cohesive cracking. In all examples, the arc length method is used to control the loading procedure. All examples in this section are solved under plane strain conditions, and the material parameters for matrix and fiber are Young's modulus $E_m = 4.6\,\text{GPa}$, $E_f = 232\,\text{GPa}$ and Poisson ratio $\nu_m = 0.4$, $\nu_f = 0.3$. In following examples, one X-VCFEM consists of 16 nodes on the cell boundary and 16 node-pairs on the interface for displacement interpolation. Before damage propagates into matrix, the stress functions

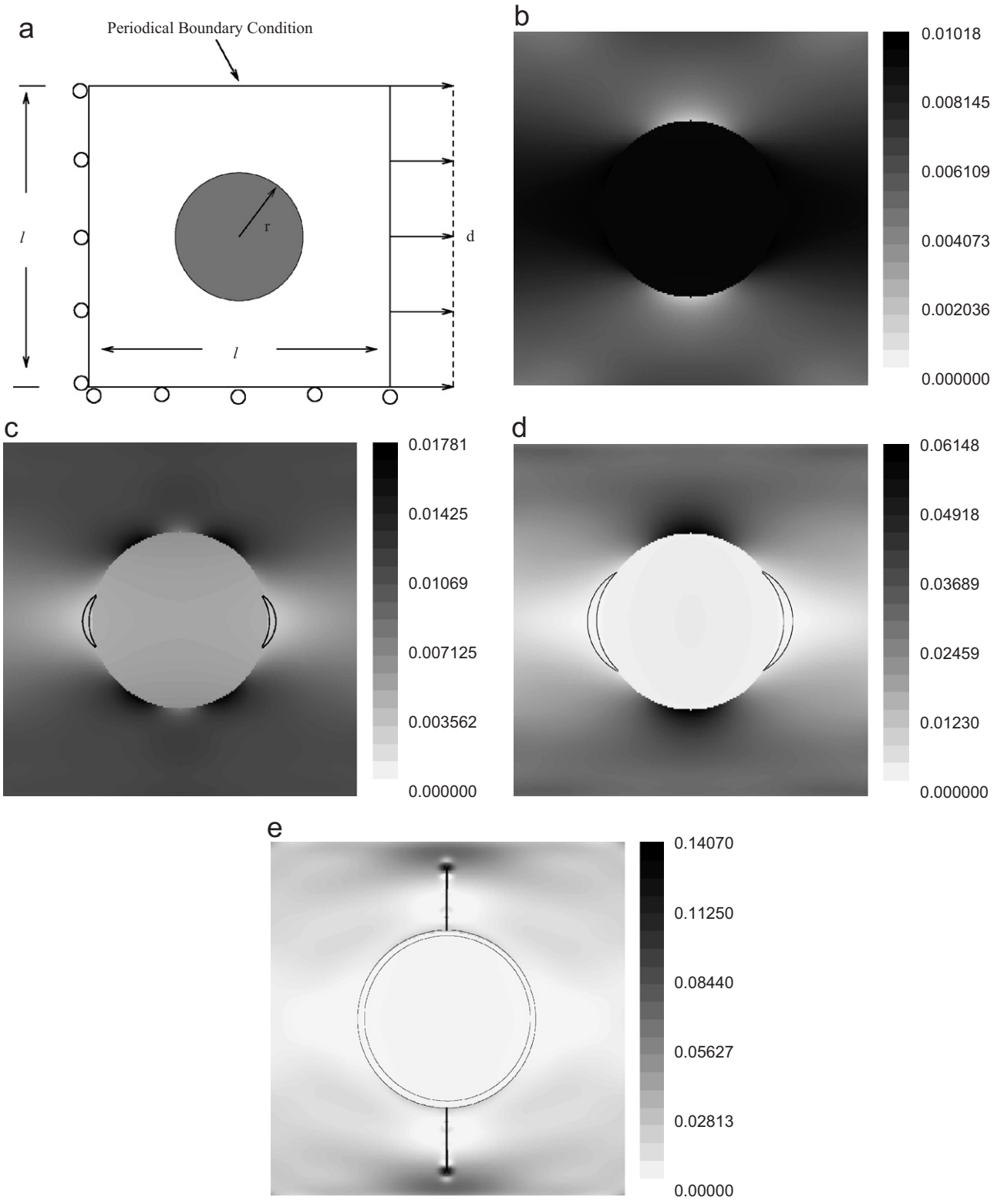

Fig. 8. (a) A square plate with one circular fiber in tension along x direction and (b–e) contour plots of the microscopic stress σ_{xx} (GPa) showing different stages of material response, viz. pre-damage, debond initiation, debonding lock and matrix cracking during damage evolution.

for matrix of one element consist of 102 terms of polynomial functions and 45 terms of reciprocal functions. After the cracks advance into matrix, one branch function and 16 wavelet functions are added into the stress interpolation for each crack. The debonded region along the interface is expressed by dark solid line in the following contour plots for all examples.

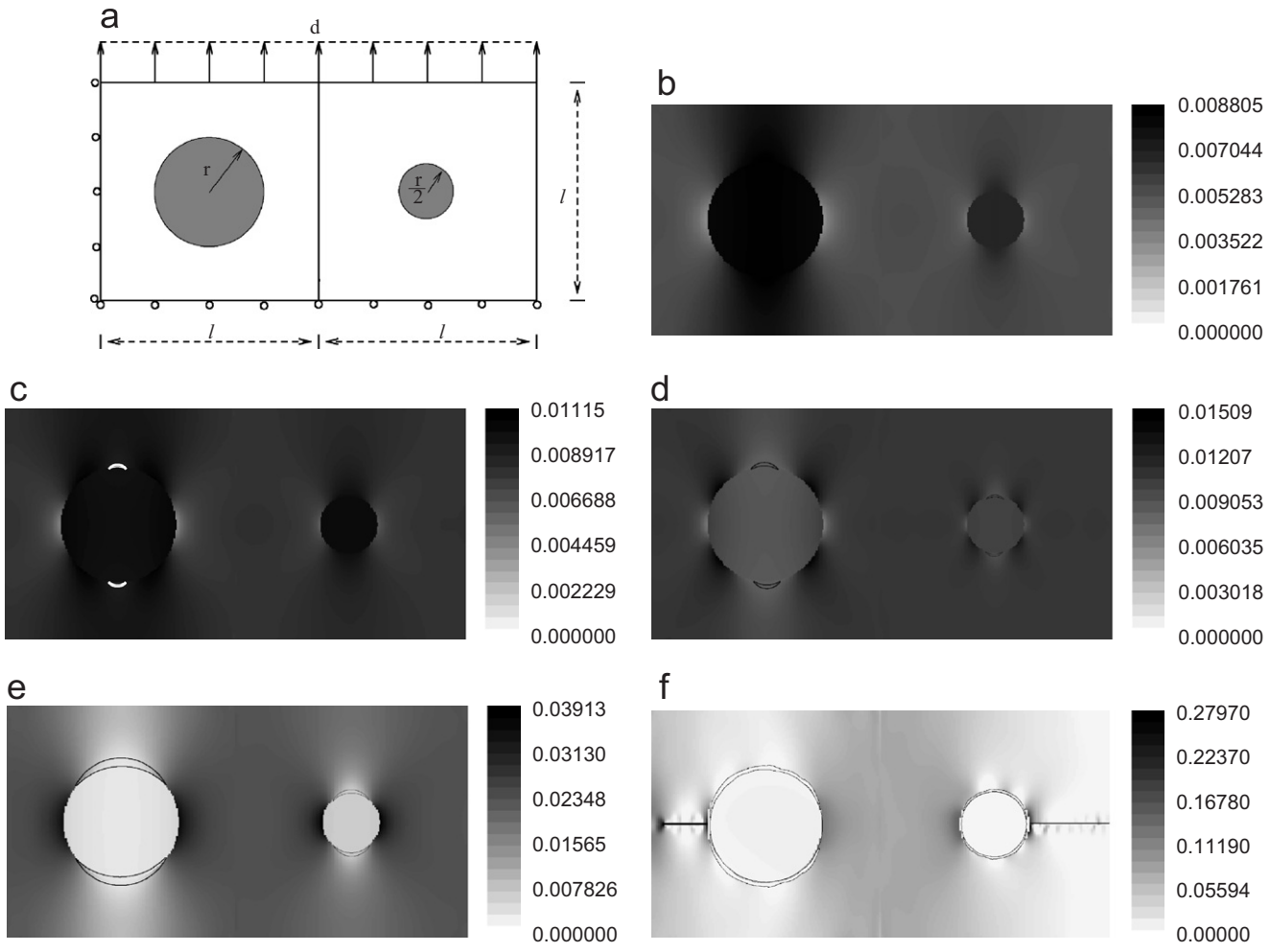

Fig. 9. (a) A plate with two circular fibers in tension along y direction. Contour plots of the microscopic stress σ_{yy} (GPa) showing different stages, viz. (b) pre-damage, (c–e) interfacial debonding, and (f) matrix cracking.

5.1. Damage evolution in microstructures containing circular fibers

In the first example, X-VCFEM shows the interfacial debonding and sequent matrix cracking in a square microstructure with a single circular fiber. The geometrical dimensions for the specimen in Fig. 8(a) are $\mathbf{l} = 20$ mm, $\mathbf{r} = 5$ mm. The interface uses the bilinear cohesive zone model with the properties $\sigma^{\mathrm{i}}_{\max} = 0.01$ GPa, $\delta_{\mathrm{c}} = 0.001$ mm, $\delta^{\mathrm{i}}_{e} = 0.02$ mm, $\beta^{\mathrm{i}} = 0.707$. The linear cohesive zone model is used to describe matrix cracking with parameters: $\sigma^{\mathrm{c}}_{\max} = 0.07$ GPa, $\delta^{\mathrm{c}}_{e} = 0.0001$ mm, and $\beta^{\mathrm{m}} = 1$. The cohesive parameters are chosen to make $\sigma^{\mathrm{m}}_{\max} > \sigma^{\mathrm{i}}_{\max}$, so that the interfacial debonding starts before matrix cracking. The entire microstructure is modeled with one X-VCFEM element. Displacement boundary conditions are shown in Fig. 8(a), with periodic boundary conditions applied to ensure the symmetry. Figs. 8(b–e) show the contour plots of the microstructural stress σ_{yy} together with evolved position of the interfacial debonding and cracks. The growth pattern of each interfacial debonding and cracks can be observed by comparing with its initial configuration in Fig. 8(a). The evolution of interfacial debonds into propagating matrix cracks is in general complicated. However, several observations are made based on the results of the simulation by this model:

- The entire deformation process consists of four phases: pre-damage with intact stiffness, interfacial debonding, debonding lock and matrix cracking. During the damage growth procedure, the normal and tangential tractions along the interface play important roles.
- In the first phase, as shown in Fig. 8(b), there is no crack in the material. The highest stress concentration happens at the interface in the horizontal direction, the direction of the external load.
- With increase in stress concentration, the interface debonding initiates in the material as shown in Fig. 8(c). In this stage, the normal traction plays a major role in the onset of debonding and propagation along the interface. As shown in Fig. 8(c), the highest stresses symmetrically appear at four diametrically opposite positions in the matrix along the interface due to the initial interface debonding. Matrix cracking might happen at these positions with high concentration of stresses.

- When the interfacial debonding angle reaches a critical value, interfacial debonding stops growing. This is the locking stage of debonding as shown in Fig. 8(d). This happens when the normal traction ceases to increase and drive the growth of the debond. Although the interfacial debond does not propagate, stress concentration in the matrix increases with increasing external load, since the debonded interface cannot transfer the load into fiber effectively. As shown in Fig. 8(d), the highest stresses appear at the top and bottom positions of the interface.
- Fig. 8(e) shows the fourth stage of deformation, where high concentrated stresses result in matrix cracking. Two cracks propagate symmetrically into matrix from the interface. The highest stresses appear at tips of cracks and the stress in fiber is released. The evolved crack path tends to align in a direction perpendicular to the applied load direction. This agrees with the observation in [20,38]. In the final stage, the interfacial debonding again starts to propagate in addition to matrix cracking. The debonding goes through the entire interface.

In the second example, the effect of the fiber size on the crack propagation is studied by considering a microstructure containing two circular fibers of different radii. The geometrical dimensions for the specimen in Fig. 9(a) are $\mathbf{l} = 10\,\text{mm}$, $\mathbf{r} = 2.5\,\text{mm}$. The interface uses the bilinear cohesive zone model with the properties $\sigma^{\text{i}}_{\max} = 0.01\,\text{GPa}$, $\delta^{\text{i}}_{\text{c}} = 0.001\,\text{mm}$, $\delta^{\text{i}}_{e} = 0.02\,\text{mm}$, $\beta^{\text{i}} = 0.707$. The linear cohesive zone model is used to describe matrix cracking with parameters: $\sigma^{\text{c}}_{\max} = 0.15\,\text{GPa}$, δ^{c}_{e}=0.0001 mm, and β^{c}=1. The displacement boundary conditions are shown in Fig. 9(a). The entire microstructure is modeled with two X-VCFEM elements. Figs. 9(b–f) show the contour plots of the microstructural stress σ_{yy} together with evolved position of the cracks at different stages of loading.

As shown in Fig. 9(b), in the first stage there are no cracks in the material and the larger fiber gives rise to a higher stress concentration in the matrix. Fig. 9(c) shows the stress distribution in the second stage, where the debonding initiates only at the interface of the left fiber with the larger radius. In this figure, debonding does not appear along the interface of the right fiber with the smaller radius yet. The reason is that the larger fiber usually results in higher stress along the interface before damage happens. Debonding propagates along the interface and at this time the smaller fiber also debonds as shown in Fig. 9(d). In this stage, there are several regions along the interface with high stress concentrations. Fig. 9(e) shows that the highest stresses appear at the horizontal positions as the interfacial debondings propagate. Subsequently, matrix cracking happens in the element with smaller fibers, instead of the element with larger fiber. Usually, higher stress concentration tends to appear on the debonded interface with smaller fiber radius. The simulation results are in agreement with this general conclusion. Fig. 9(f) shows the contour plots of the microstructural stress at the final stage of loading, where two cracks are growing in the matrix.

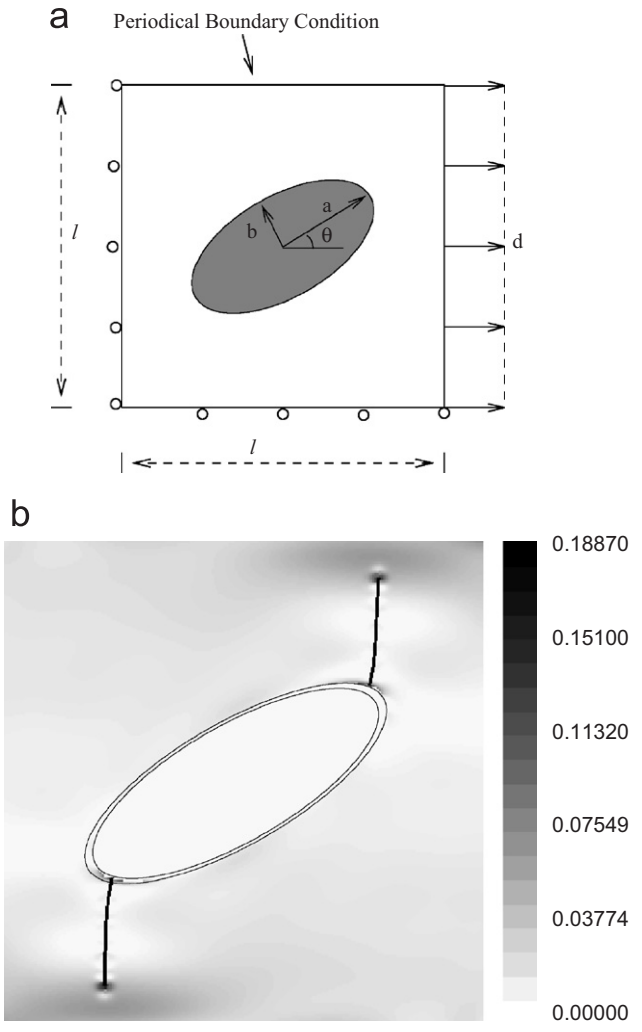

Fig. 10. (a) A square plate with a single elliptical fiber in tension along x direction and (b) contour plot of the microscopic stress σ_{xx} (GPa).

5.2. Study on the effect of fiber shape on damage growth

The effect of fiber shape on damage growth is studied with X-VCFEM in this example. The geometrical dimensions of the specimen in Fig. 10(a) are $\mathbf{l} = 20\,\text{mm}$, $\mathbf{a} = 7\,\text{mm}$, $\mathbf{b} = 2.5\,\text{mm}$, and θ=30°. The interface uses the bilinear cohesive zone model with the properties $\sigma^{\text{i}}_{\max} = 0.01\,\text{GPa}$, $\delta_{\text{c}} = 0.001\,\text{mm}$, $\delta^{\text{i}}_{e} = 0.02\,\text{mm}$, $\beta^{\text{i}} = 0.707$. The linear cohesive zone model is used to describe matrix cracking with parameters: $\sigma^{\text{c}}_{\max} = 0.07\,\text{GPa}$, $\delta^{\text{c}}_{e} = 0.0001\,\text{mm}$, and $\beta^{\text{c}} = 1$. The displacement boundary conditions are shown in Fig. 10(a). The microstructure is modeled with a single X-VCFEM element. Fig. 10(b) shows the contour plots of the microstructural stress σ_{yy} along with the evolved crack configurations. This damage process again goes through three stages, viz. interfacial debonding, debonding locking and matrix cracking. The cracks propagate symmetrically and tend to be perpendicular to the major load direction. However, the crack initiation positions are not at the tips of the ellipse due to the 30° orientation of the fiber. The reason is that the nonzero

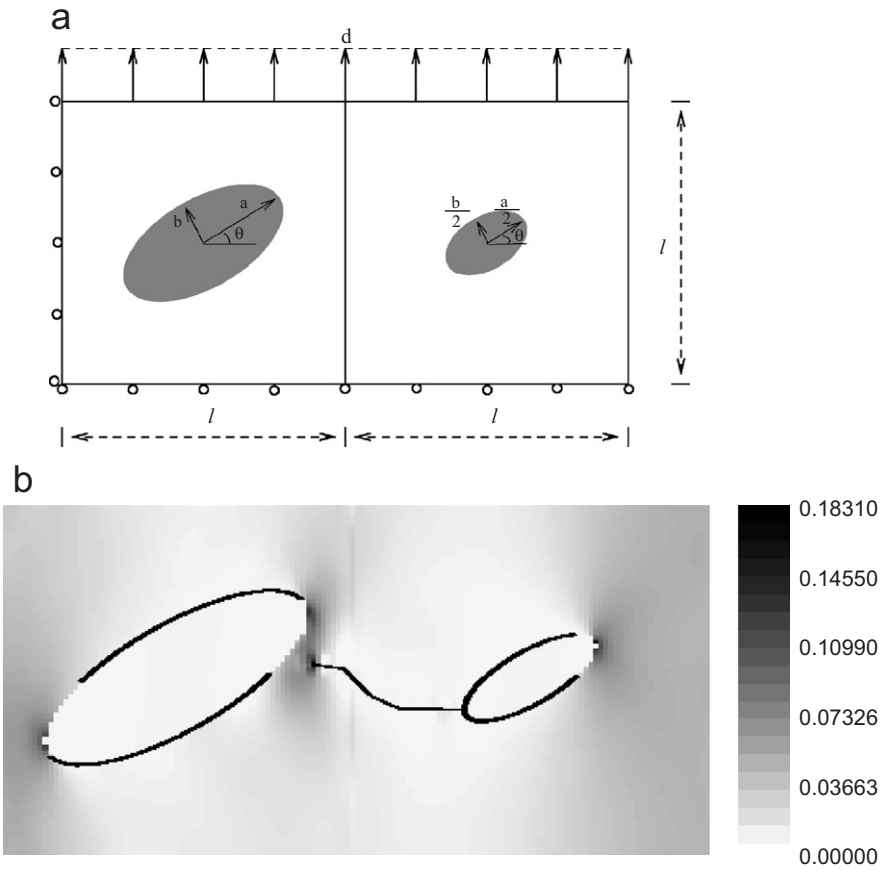

Fig. 11. (a) A plate with two elliptic fibers in tension along y direction and (b) contour plot of the microscopic stress σ_{yy} (GPa).

orientation results in the highest stress concentration deflecting from the tip of the ellipse, during the debond locking stage. This example shows that the initial matrix cracking position at the interface depends on the external load, fiber orientation, fiber shape, etc. Finally, the entire interface is debonded rendering the effective fiber position as a void.

The effect of shape and size of fibers are also studied in the next example, where the specimen includes two different size elliptical fibers. The geometrical dimensions for the specimen in Fig. 11(a) are $\mathbf{l} = 10\,\text{mm}$, $\mathbf{a} = 4.2\,\text{mm}$, $\mathbf{b} = 1.5\,\text{mm}$, and $\theta = 30°$. The interface uses the bilinear cohesive zone model with the properties $\sigma^{\text{i}}_{\max} = 0.01\,\text{GPa}$, $\delta_{\text{c}} = 0.001\,\text{mm}$, $\delta^{\text{i}}_{e} = 0.02\,\text{mm}$, $\beta^{\text{i}} = 0.707$. The linear cohesive zone model is used to describe matrix cracking with parameters: $\sigma^{\text{c}}_{\max} = 0.15\,\text{GPa}$, $\delta^{\text{c}}_{e} = 0.0001\,\text{mm}$, and $\beta^{\text{c}} = 1$. The displacement boundary conditions are shown in Fig. 11(a). Fig. 11(b) shows the contour plots of the microstructural stress σ_{yy} together with evolved position of the cracks. Interfacial debonding starts from the interface of the larger fiber and grows along the interface. Then the interface of the smaller fiber also goes into softening and initiates debonding. The simulation shows that the high stress concentrations appear at the left part of the interface of the smaller fiber, which leads to the crack branching into matrix between the two fibers. The propagated crack crosses the element boundary, goes through another element, and tends to connect the two debonded interfaces.

6. Concluding remarks

The X-VCFEM is enhanced in this paper to combine two simultaneous modes of damage, viz. interfacial debonding and matrix cracking and predict the damage propagation from the interface into the matrix. Polynomial functions, reciprocal functions, branch functions and wavelet functions are made to the element stress interpolations to accurately depict the stress discontinuities and concentrations at interfaces and cracks. A criterion for assessing the crack advancing into matrix is proposed, which is based on the energy release rate and cohesive energy. Effectiveness of X-VCFEM is demonstrated in several numerical examples. Also, X-VCFEM is extended to study effects of microstructural morphological characteristics, such as fiber shape, fiber orientation, and relative sizes, etc., on failure properties.

Acknowledgments

This work has been partially supported by the Air Force Office of Scientific Research through Grant No. F49620-98-1-01-93 (Program Director: Dr. B.L. Lee) and by the Army Research Office through Grant No. DAAD19-02-1-0428 (Program Director: Dr. B. Lamattina). This sponsorship is gratefully acknowledged. Computer support by the Ohio Supercomputer Center through Grant PAS813-2 is also gratefully acknowledged.

References

[1] R.S. Barsoum, On the use of isoparametric finite elements in linear fracture mechanics, Int. J. Numer. Methods Eng. 10 (1976).

[2] R.D. Henshelland, K.G. Shaw, Crack tip finite elements are unnecessary, Int. J. Numer. Methods Eng. 9 (1975).

[3] H.D. Hibbit, Some properties of singular isoparametric element, Int. J. Numer. Methods Eng. 11 (1977).

[4] Y. Yamamoto, N. Tokuda, Determination of stress intensity factor in cracked plates by the finite element method, Int. J. Numer. Methods Eng. 6 (1973).

[5] Y. Yagawa, T. Aizawa, Y. Ando, Crack analysis of power hardening materials using a penalty function and superposition method, Proceedings of 12th Conference Fracture Mechanics, ASTM STP, vol. 700, 1980.

[6] P. Tong, T.H.H. Pian, S.J. Lasry, A hybrid-element approach to crack problems in plane elasticity, Int. J. Numer. Methods Eng. 7 (1973).

[7] R. Piltner, Special finite elements with holes and internalcracks, Int. J. Num. Methods Eng. 21 (1985).

[8] A. Needleman, A continuum model for void nucleation by interfacial debonding, J. Appl. Mech. 54 (1987).

[9] V. Tvergaard, Effect of fiber debonding in a whisker-reinforced metal, Mater. Sci. Eng. A 125 (1990).

[10] D.C. Lo, D.H. Allen, Modeling of delamination damage evolution on laminated composites subjected to low velocity impact, Int. J. Damage 3 (1994).

[11] C.J. Lissenden, C.T. Herakovich, Numerical modeling of damage development and viscoplasticity in metal matrix composites, Comput. Methods Appl. Mech. Eng. 126 (1995).

[12] P. Tong, A hybrid crack element for rectilinear anisotropic material, Int. J. Numer. Methods Eng. 11 (1977).

[13] S. Ghosh, Y. Ling, M. Bhaskar, K. Ran, Interfacial debonding analysis in multiple fiber reinforced composites, Mech. Mater. 32 (2000).

[14] S. Moorthy, S. Ghosh, A model for analysis for arbitrary composite and porous microstructures with voronoi cell finite elements, Int. J. Numer. Methods Eng. 39 (1996).

[15] S. Moorthy, S. Ghosh, Adaptivity and convergence in the voronoi cell finite element model for analyzing heterogeneous materials, Comput. Meth. Appl. Mech. Eng. 185 (2000).

[16] S. Ghosh, S. Moorthy, Particle cracking simulation in non-uniform microstructures of metal-matrix composites, Acta Metal. Mater. 46 (3) (1998).

[17] S. Ghosh, S.N. Mukhopadhyay, A two dimensional automatic mesh generator for finite element analysis of randomly dispersed composites, Comput. Struct. 41 (2) (1991).

[18] S. Ghosh, S. Moorthy, Three dimensional voronoi cell finite element model for modeling microstructures with ellipsoidal heterogeneities, Comput. Mech. 34 (6) (2004).

[19] S. Li, S. Ghosh, Debonding in composite microstructures with morphologic variations, Int. J. Comput. Methods 1 (1) (2004).

[20] S. Li, S. Ghosh, Extended voronoi cell finite element model for multiple cohesive crack propagation in brittle materials, Int. J. Numer. Methods Eng. 65 (2006).

[21] B.K. Ahn, W.A. Curtin, T.A. Parthasarathy, R.E. Dutton, Criteria for crack deflection/penetration criteria for fiber-reinforced ceramic matrix composites, Compos. Sci. Technol. 58 (1998).

[22] M.Y. He, C.H. Hsueh, P.H. Becher, Deflection versus penetration of a wedge-loaded crack: effects of branch-crack length and penetrated-layer width, Compos. Part B Eng. 31 (2000).

[23] M.Y. He, J.W. Hutchinson, Crack deflection at an interface between dissimilar elastic materials, Int. J. Solids Struct 25 (9) (1989).

[24] A.A. Mammoli, A.L. Graham, I.E. Reimanis, D.L. Tullock, The effect of flaws on the propagation of cracks at bi-materials interfaces, Acta Metall. Mater. 43 (3) (1995).

[25] G.I. Barenblatt, The mathematical theory of equilibrium cracks in brittle fracture, Adv. Appl. Mech. 7 (1962).

[26] D.S. Dugdale, Yielding in steel sheets containing slits, J. Mech. Phys. Solids 8 (1960).

[27] A. Needleman, An analysis of decohesion along an imperfect interface, Int. J. Fract. 42 (1990).

[28] A. Needleman, Micromechanical modeling of interfacial decohesion, Ultramicroscopy 40 (1992).

[29] J.W. Foulk, D.H. Allen, K.L.E. Helms, Formulation of a three-dimensional cohesive zone model for application to a finite element algorithm, Comput. Methods Appl. Mech. Eng. 183 (2000).

[30] P.H. Geubelle, Finite deformation effects in homogeneous and interfacial fractur, Int. J. Solids Struct. 32 (1995).

[31] M. Ortiz, A. Pandolfi, Finite-deformation irreversible cohesive element for three-dimensional crack-propagation analysis, Int. J. Numer. Methods Eng. 44 (1999).

[32] G.T. Camacho, M. Ortiz, Computational modeling of impact damage in brittle materials, Int. J. Solids Struct. 33 (1996).

[33] T. Belytschko, Y. Krongauz, D. Organ, M. Fleming, P. Krysl, Meshless methods: an overview and recent developments, Comput. Methods Appl. Mech. Eng. 139 (1996).

[34] M. Elices, G.V. Guinea, J. Gomez, J. Planas, The cohesive zone model: advantages limitations and challenges, Eng. Fract. Mech. 69 (2002).

[35] M.A. Crisfield, A fast incremental/iterative solution procedure that handles 'snap-through', Comput. Struct. 13 (1981).

[36] M.A. Crisfield, An arc-length method including line searches and accelerations, Int. J. Numer. Methods Eng. 19 (1983).

[37] K.H. Schweizerhof, Y. Wriggers, Consistent linearization for path following methods in nonlinear f.e. analysis, Comput. Meth. Appl. Mech. Eng. 59 (1986).

[38] S. Li, S. Ghosh, Multiple cohesive crack propagation by the extended Voronoi cell finite element model, Int. J. Fracture 141 (3–4) 2006.

[39] S. Mariani, U. Perego, Extended finite element method for quasi-brittle fracture, Int. J. Numer. Methods Eng. 58 (2003).